Available online at www.sciencedirect.com
ScienceDirect
Cement and Concrete Research 36 (2006) 1679–1685
Cement and Concrete Research

Behavior of high strength concrete with and without steel fiber reinforcement in triaxial compression

Xiaobin Lu [a,*], Cheng-Tzu Thomas Hsu [b,1]

[a] The Thornton and Tomasetti Group, 24 Commerce Street, 8th floor, Newark, NJ 07102, USA
[b] Department of Civil and Environmental Engineering, New Jersey Institute of Technology, Rm. 213 Colton Hall, University Heights, Newark, NJ 07102, USA

Received 1 August 2005; accepted 29 May 2006

Abstract

Based on an extensive experimental program, this paper studies the behavior of high strength concrete and steel fiber reinforced high strength concrete under uniaxial and triaxial compression. Triaxial stress–strain relations and failure criteria are used to evaluate the effect of steel fiber reinforcement on the mechanical properties of high strength concrete in triaxial compression, which is found to be insignificant.

Keywords: Compressive strength; Concrete; Fiber reinforcement; Mechanical properties; Triaxial compression

1. Introduction

High strength concrete has been widely used in the construction practice around the world despite the fact that it has a relatively low tensile strength and weak deformation capability, also known as brittleness. It is generally accepted that the ductility of high strength concrete can be improved by introducing various types of fibers, especially steel fibers, into the concrete mix. However, just like the steel bars in the reinforced concrete, the steel fibers can only contain the development of the cracks, but cannot totally eliminate the concrete cracking. Therefore, in the case where the cracking of concrete is restrained by the other sources, such as the confining stress under triaxial compression, the effect of adding steel fiber reinforcement to the concrete mix is questionable.

Although a lot of research has been performed on the multiaxial behavior of both high strength concrete [1–3] and steel fiber reinforced high strength concrete [4,5], the comparison between the nonlinear stress–strain relations of those two materials and the difference between their ultimate failure criteria haven't been well addressed. Therefore, focusing on those two aspects, the purpose of this paper is to evaluate the effect of steel fiber reinforcement on the behavior of high strength concrete under triaxial compression.

2. Experimental program

2.1. Mix proportions

Two types of concrete were used in this study, high strength concrete and fiber reinforced high strength concrete with 1.0% volume ratio of steel fiber (hereinafter designated as HSC and SFHSC, respectively). The concrete mix proportions are listed in Table 1. Type I cement, 10 mm crushed gravel satisfying ASTM C33 gradation requirement, and ASTM No. 2 grade river sand were employed for all the mixes. Hook-ended 30-mm-long steel fibers with a diameter of 0.5 mm were used. To achieve good workability, highly effective super-plasticizer was introduced to each of the fresh mixes. At the age of 21 days, the specimens were taken out of the curing room and carefully ground on both ends to provide the flat and smooth bearing areas for the loading platens, and then they were taken back to the curing room until the testing age.

2.2. Lubricated loading platen

As indicated by many researchers [6–8], the end constraint induced by the friction between the rigid loading platen and the

* Corresponding author. Tel.: +1 973 286 6222; fax: +1 973 286 6223.
E-mail addresses: xl7@njit.edu (X. Lu), hsuc@adm.njit.edu (C.-T.T. Hsu).
[1] Tel.: +1 973 596 2472; fax: +1 973 596 5790.

0008-8846/$ - see front matter © 2006 Elsevier Ltd. All rights reserved.
doi:10.1016/j.cemconres.2006.05.021

Table 1
Mix proportions of HSC and SFHSC

	Water–cement ratio	Water (kg/m^3)	Cement (kg/m^3)	Sand (kg/m^3)	Coarse aggregate (kg/m^3)	Superplasticizer (L/m^3)	Slump (mm)
HSC	0.33	170	520	760	1000	4.3	235
SFHSC	0.33	170	520	760	1000	4.3	100

specimen has a significant influence on the mechanical properties of concrete under uniaxial compression. In an attempt to minimize this effect for this study, the rigid loading platen was lubricated with a combination of two 0.125-mm-thick teflon sheets on top of one layer of 0.015 mm thick aluminum foil. The aluminum foil was put directly on the specimen end to prevent the possible reverse end condition [7,8] caused by the bearing grease applied between the teflon sheet and the foil. Under uniaxial compression, reference [9] indicated that this lubricated platen could produce the same compressive strength for 100-mm-diameter cylinders with different h/d ratios of 1/1, 1.5/1 and 2/1, and that the concrete cylinder showed a splitting tensile failure pattern (Fig. 1). This pattern was shown by Mindess et al. [8] to be the theoretical failure mode of a true uniaxial compression, rather than the typical cone failure. It was also found that under this lubricated loading platen, the 100 mm × 150 mm cylinder was more likely to exhibit a uniform lateral expansion along the entire cylinder height, a good indication of true uniaxial compression. Therefore, this setup was adopted for the uniaxial compression test.

2.3. Triaxial compression test setup

The triaxial compression tests were performed by the MTS 810 material testing system (Fig. 2), a rigid frame MTS servo-hydraulic closed loop testing machine with a frame stiffness rated at 11.0×10^9 N/m. It has a 4450 kN load capacity and the triaxial cell is able to apply up to 84 MPa confining pressure.

A confining pressure intensifier is used to fill and pressurize the triaxial cell with the confining fluid, and the confining pressure σ_3 is directly measured by a pressure transducer inside the intensifier. The axial load is applied by the axial actuator and

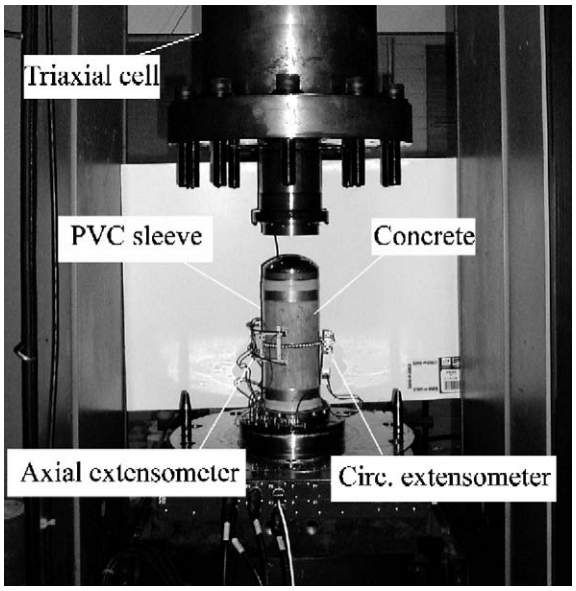

Fig. 2. Triaxial compression test setup.

an in-vessel load cell records the axial deviatoric load F_0. The actual axial stress σ_1 acting on the concrete can then be obtained as $F_0/A_s+\sigma_3$, where A_s is the cross-sectional area of the concrete cylinder. The axial actuator and the confining pressure intensifier can be programmed together to provide the desired load paths.

Clip gages (axial and circumferential extensometers, Fig. 2) were used to measure the deformation since they have an advantage over electrical strain gages in capturing the average deformation for a much larger portion of concrete. This is especially desirable in obtaining the total circumferential deformation along the whole perimeter of the cylinder, which is then used to derive the average lateral strain ε_3 of concrete.

To prevent penetration of the pressurized oil through the concrete, a PVC transparent heat-shrink tubing with an initial inside diameter of 102 mm and a thickness of 1.85 mm was adopted as the isolation sleeve for concrete cylinders in the triaxial chamber. The tensile capacity of the tubing is well above

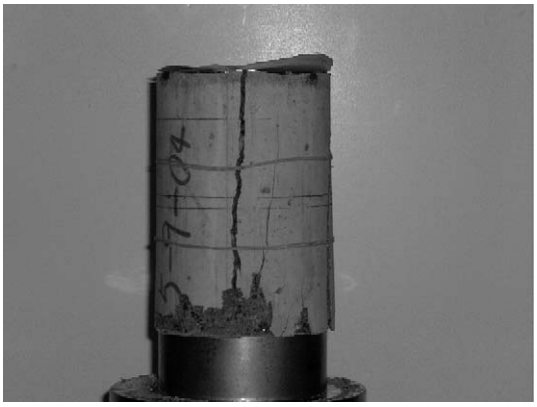

Fig. 1. Splitting tensile failure under lubricated loading platen in uniaxial compression.

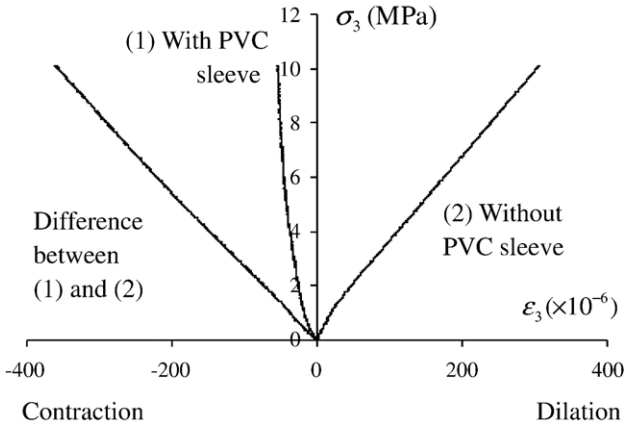

Fig. 3. Lateral strain caused by the thickness change of the PVC sleeve under different confining pressures.

Fig. 4. Triaxial compression of 100×200 mm cylinder under rigid loading platen. (Left: after test, Right: before test).

50% and the ultimate tensile strength is around 50 MPa. For only 5 min under 150 °C, this tube can shrink and tightly wrap around the side surface of the cylinder. The thickness change of the tubing under different confining pressures must be taken into account in calculating the lateral strains of the concrete cylinder from the measurements of the circumferential extensometer. This was done by performing two separate triaxial compression tests on a specimen-size solid steel rod, with and without the PVC sleeve, using the same loading scheme. The result is shown in Fig. 3. The first and second curves represent the lateral strains of the rod with and without the PVC tubing under the same loading condition, respectively, and therefore the difference between them is the lateral strains caused by the thickness decrease of the tubing under confining pressures, which should be added to the reading of the circumferential extensometer to get the true lateral strains of the concrete cylinder under triaxial compression.

As in the case of the uniaxial compression, the 100 mm×150 mm cylinder with the lubricated loading platen was also adopted in the triaxial compression test to minimize the considerable end effect induced by a much higher axial load. Additionally, triaxial compression tests for 100 mm×200 mm standard concrete cylinders under rigid loading platen were also

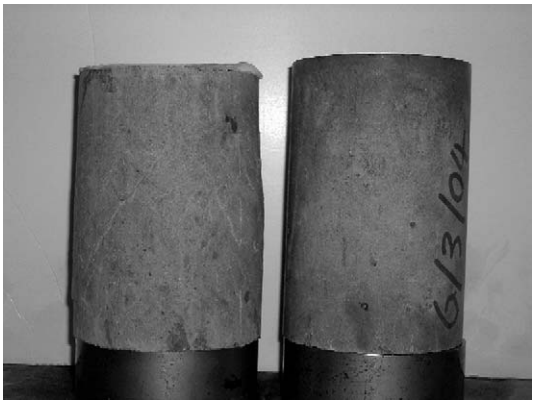

Fig. 5. Triaxial compression of 100×150 mm cylinder under lubricated loading platen. (Left: after test, Right: before test).

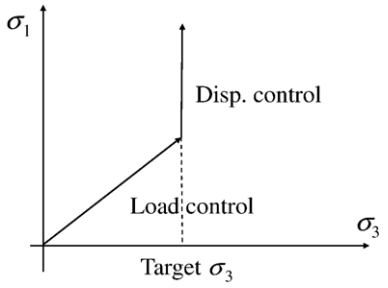

Fig. 6. Load path T-1 and T-2 in triaxial compression.

conducted to compare the results. In the latter case, an apparent swelling occurred around the mid-height of the cylinder (Fig. 4) while both ends remained almost unchanged, indicating the big end constraint imposed by the rigid platen. As expected, the lubricated platen provided a fairly uniform lateral expansion of the cylinder (Fig. 5). Ref. [9] showed that the ultimate axial strength σ_{1c} and stress–strain relations under triaxial compression for those two cases were essentially the same, which might be attributed to the high lateral confining pressure which counterbalanced the end constraint effect. In both cases, shear type failure manifested by inclined concrete cracks can be clearly seen on the concrete surface.

2.4. Loading schemes

Under uniaxial compression, a displacement control with a rate of 0.005 mm/s was employed to obtain the entire stress–strain curve (including the descending branch). Under triaxial compression, two different load paths, T-1 and T-2, were employed (Fig. 6). The difference between T-1 and T-2 is the σ_3/σ_1 ratio before the target confining pressure σ_3 is reached, where σ_1 is the axial stress and σ_3 is the confining pressure. This ratio is 1:2 for T-1 and 1:6 for T-2, respectively. In both paths, load control was employed before the target confining pressure was obtained with an increasing rate of σ_3 of 7 MPa/min and 3–4 MPa/min for T-1 and T-2, respectively. After the target σ_3 was reached, both paths adopted displacement control with a rate from 0.005 mm/s to 0.006 mm/s all the way until the failure (including strain softening) of the specimen. Load path

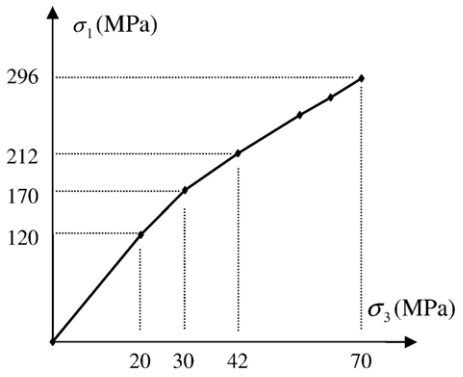

Fig. 7. Load path T-2′ in triaxial compression.

Table 2
Triaxial compression results of HSC

Load path	Confining pressure σ_3 (MPa)	Peak axial stress σ_{1c} (MPa)	Peak lateral strain ε_{3c} ($\times 10^{-6}$)	Peak axial strain ε_{1c} ($\times 10^{-6}$)
Uniaxial	0	67	−1000	2514
T-1	3.5	84.9	−2168	4660
T-1	7	99	−3609	7759
T-1	14	130.7	−5209	12,373
T-2	14	132.7	−4649	12,515
T-2	14	134.9	−5846	13,454
T-2	14	135.5	−5440	13,728
T-1	21	154	−5739	16,609
T-2	21	157.1	−6547	18,257
T-2	21	161.2	−7782	19,429
T-1	28	180.2	−8679	25,007
T-2	28	179.9	−8865	24,089
T-1	42	229.1	−11,084	32,130
T-1	56	276	−12,376	40,582

T-2′ was derived from T-2 for the application of high target confining pressures from 42 MPa to 70 MPa (Fig. 7). In load path T-3, the axial stress σ_1 was first increased to 40% of the uniaxial compressive strength without any confining pressure, and then σ_1 and $\sigma_3$were increased simultaneously at the same rate until the target confining pressure was reached. Right after this point, displacement control was adopted. For the cyclic loading, the unloading took the load control mode with a decreasing rate of axial stress σ_1 of 40 MPa/min and a constant confining pressure σ_3. After axial stress was reduced to the target value, the control mode was switched back to the previous displacement control again all the way up to the next load cycle.

3. Results and analyses

In this section, the compressive strain is designated as positive.

Table 3
Triaxial compression results of SFHSC

Load path	Confining pressure σ_3 (MPa)	Peak axial stress σ_{1c} (MPa)	Peak lateral strain ε_{3c} ($\times 10^{-6}$)	Peak axial strain ε_{1c} ($\times 10^{-6}$)
Uniaxial	0	69.0	−1361	2777
T-2	7	105.2	−3472	7082
T-2	14	136.8	−5440	12,711
T-2	14	139.0	−4625	12,090
T-2	21	164.1	−6750	16,973
T-2	21	162.3	−8011	20,195
T-2	28	186.5	−9165	25,722
T-2′	28	189.6	−13,145[a]	27,439[a]
T-1	28	191.6	−9858	24,379
T-3	28	191.8	−9866	24,053
T-2	28	189.6	−9748	25,230
T-2′	42	239.0	−12,313	33,259
T-2′	56	282.2	−13,867	42,168
T-2′	63	308.2	−15,497	45,089
T-2′	70	324.1	17,338	48,203

[a] Abnormal strain values.

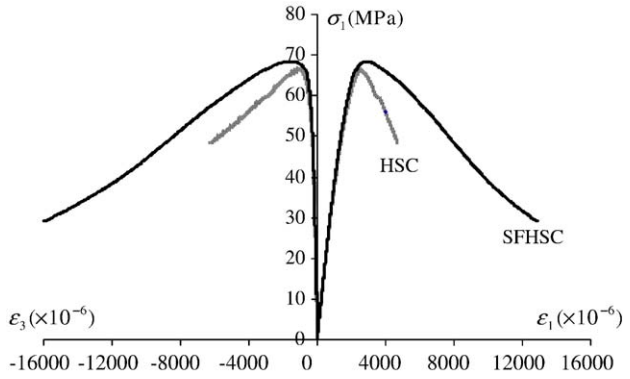

Fig. 8. Stress–strain curves of HSC and SFHSC in uniaxial compression.

3.1. Uniaxial compression

With the introduction of the steel fiber reinforcement, the uniaxial compressive strength (under lubricated loading platen) of HSC was increased from 67.0 MPa to 69.0 MPa, and the axial and lateral strains at peak stress (ε_{1c} and ε_{3c}) were also increased (see Tables 2 and 3). Although the stress–strain curves followed the same trend on the ascending branch, the SFHSC was more ductile than HSC on the descending branch (Fig. 8). The HSC experienced a brittle splitting tensile failure (Fig. 1) when the lateral deformation exceeded its tensile capacity, while the SFHSC exhibited more ductility without a sudden breakage of the cylinder, which could be attributed to the improved tensile capacity of HSC with the steel fiber reinforcement.

3.2. Triaxial compression

The triaxial compression test results for HSC and SFHSC under different confining pressures and load paths are listed in Tables 2 and 3.

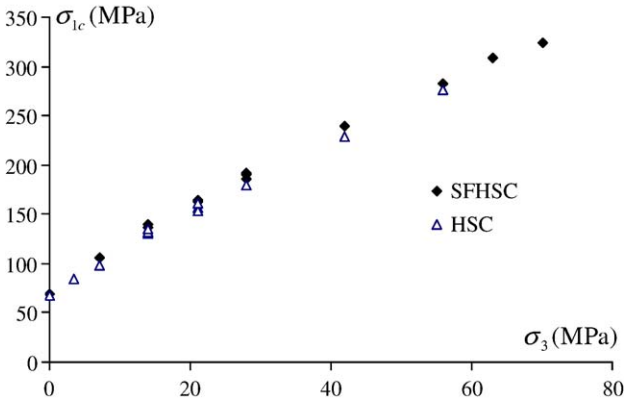

Fig. 9. Mohr-Coulomb failure criterion for HSC and SFHSC.

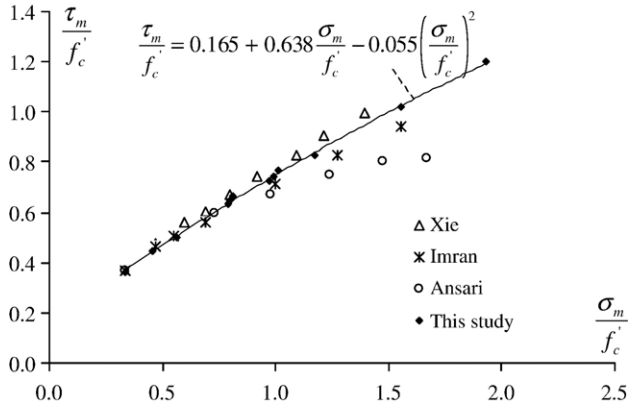

Fig. 10. Comparison of compressive meridians of HSC from different studies.

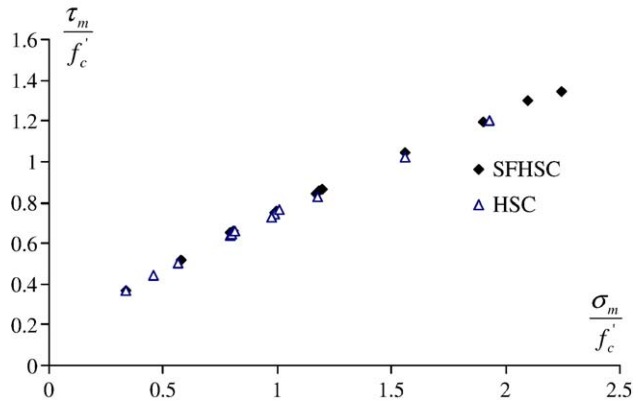

Fig. 12. Comparison of compressive meridians of HSC and SFHSC.

3.2.1. Mohr-Coulomb failure criterion

The Mohr-Coulomb failure criterion can be expressed as Eq. (1):

$$\frac{\sigma_1}{f_c'} = 1 + k\frac{\sigma_3}{f_c'} \tag{1}$$

where σ_1 denotes the axial stress; σ_3 denotes the confining pressure; f_c' denotes the uniaxial compressive strength; $k = \frac{1+\sin\phi}{1-\sin\phi}$ and ϕ represents the internal-friction angle of concrete.

The k values for concrete with various strength grades from previous research are highly scattered from 2.6 to 5.3 [1–4,11,12]. In this study, it was found that k is 4.0 and 3.95 for HSC and SFHSC, respectively, and it can be seen from Fig. 9 that there is no obvious difference in terms of the failure envelop between HSC and SFHSC. The internal-friction angle ϕ of both HSC and SFHSC can be adopted as 37°, indicating a trivial effect of the steel fiber reinforcement on this parameter.

3.2.2. Willam-Warnke failure criterion

The 5-parameter model of the Willam-Warnke failure criterion [10] is now widely used in the concrete model analysis. It has been adopted by the popular finite element analysis software ANSYS. The meridian equation takes the following form:

$$\frac{\tau_m}{f_c'} = a_0 + a_1\frac{\sigma_m}{f_c'} + a_2\left(\frac{\sigma_m}{f_c'}\right)^2 \tag{2}$$

where in Eq. (2) the average normal stress $\sigma_m = I_1/3 = (\sigma_1 + \sigma_2 + \sigma_3)/3$; the mean shear stress $\tau_m = \frac{1}{\sqrt{15}}[(\sigma_1-\sigma_2)^2 + (\sigma_2-\sigma_3)^2 + (\sigma_3-\sigma_1)^2]^{1/2}$; and σ_1, σ_2 and σ_3 denote the stresses in the three principal directions.

From this study, the compressive meridian of HSC can be expressed as Eq. (3):

$$\frac{\tau_m}{f_c'} = 0.165 + 0.638\frac{\sigma_m}{f_c'} - 0.055\left(\frac{\sigma_m}{f_c'}\right)^2 \tag{3}$$

Fig. 10 shows the comparison of the compressive meridians of different HSCs with comparable compressive strengths from this study (f_c'=67.0 MPa) and previous research including Xie et al. [1] (f_c'=60.2 MPa), Imran and Pantazopoulou [3] (f_c'=73.4 MPa) and Ansari and Li [2] (f_c'=72.2 MPa).

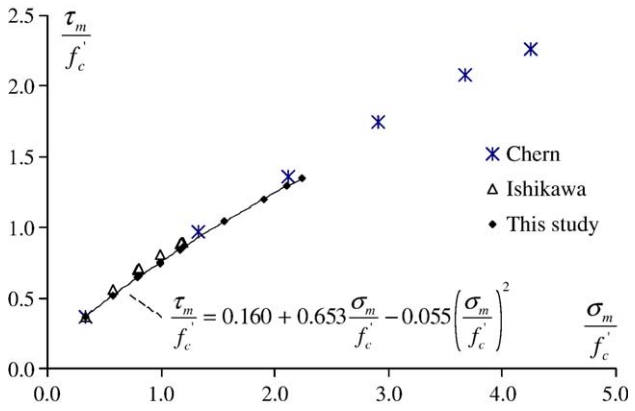

Fig. 11. Comparison of compressive meridians of SFHSC from different studies.

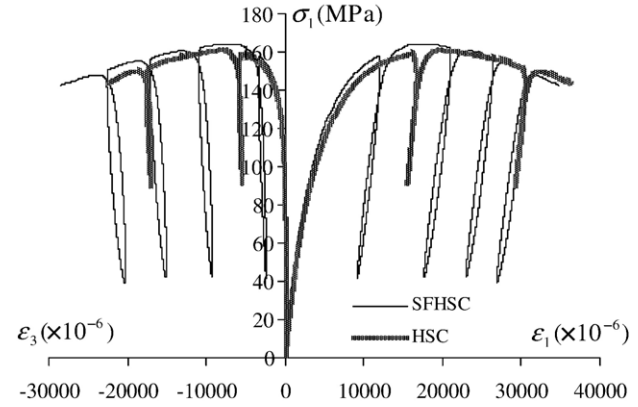

Fig. 13. Triaxial stress–strain curves of HSC and SFHSC under load path T-2 and confining pressure σ_3=21 MPa.

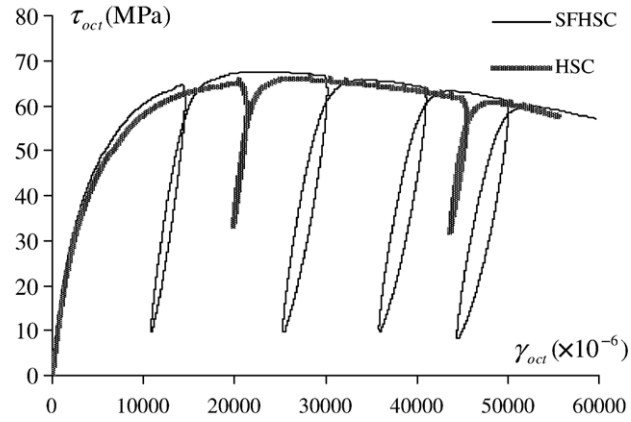

Fig. 14. Octahedral shear stress–strain curves of HSC and SFHSC under load path T-2 and confining pressure σ_3=21 MPa.

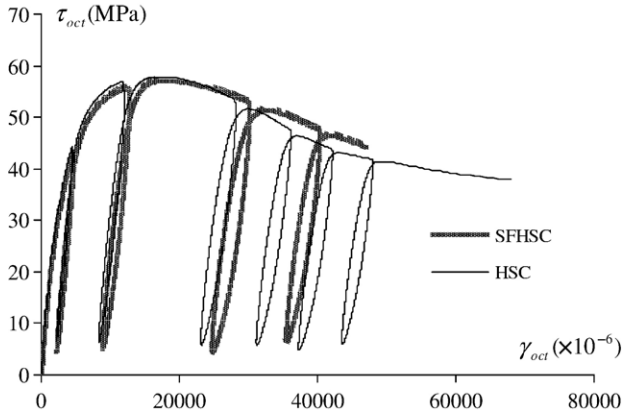

Fig. 16. Octahedral shear stress–strain curves of HSC and SFHSC under load path T-2 and confining pressure σ_3=14 MPa.

The compressive meridian of SFHSC takes the following form:

$$\frac{\tau_m}{f_c'} = 0.160 + 0.653\frac{\sigma_m}{f_c'} - 0.055\left(\frac{\sigma_m}{f_c'}\right)^2 \quad (4)$$

Fig. 11 shows the comparison of the compressive meridians of the concrete with steel fiber reinforcement from Eq. (4) of this study (f_c'=69.0 MPa) and studies of Chern et al. [4] (f_c'= 25 MPa) and Ishikawa et al. [5] (f_c'=81 MPa). Although the strengths are quite different, the compressive meridian of each of the fiber reinforced concrete essentially falls within the same envelope.

If all the compressive meridian data points of both HSC and SFHSC obtained in this study are put together (Fig. 12), it can be found that the difference between them is quite small. Therefore a uniform compressive meridian can be adopted for both of them.

3.2.3. Triaxial stress–strain relations

Fig. 13 shows the comparison between the triaxial stress–strain curves of HSC and SFHSC under load path T-2 and the confining pressure σ_3=21 MPa. Fig. 14 shows the octahedral shear stress–strain curves under the same condition, where the octahedral shear stress $\tau_{oct} = \frac{1}{3}\sqrt{(\sigma_1-\sigma_2)^2+(\sigma_2-\sigma_3)^2+(\sigma_3-\sigma_1)^2}$ and the engineering octahedral shear strain $\gamma_{oct} = \frac{2}{3}\sqrt{(\varepsilon_1-\varepsilon_2)^2+(\varepsilon_2-\varepsilon_3)^2+(\varepsilon_3-\varepsilon_1)^2}$. Figs. 15 and 16 are the corresponding curves for the same load path and the confining pressure σ_3=14 MPa. It can be found from those figures that HSC and SFHSC behave with a similar nonlinear stress–strain relationship under triaxial compression. Unlike the uniaxial compression, the introduction of steel fiber reinforcement has no significant influence on the triaxial strength and the ductility of HSC.

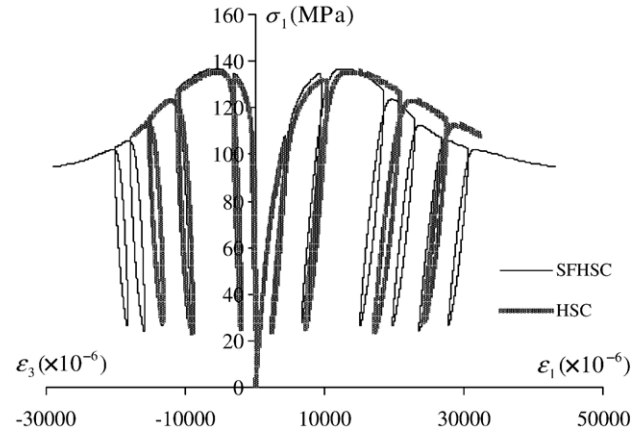

Fig. 15. Triaxial stress–strain curves of HSC and SFHSC under load path T-2 and confining pressure σ_3=14 MPa.

Fig. 17 shows the relationship between the ratio $\frac{\varepsilon_{1c}}{\varepsilon_{cu}}$, where ε_{1c} and ε_{cu} represent the axial strain at peak stress in triaxial and uniaxial compression, respectively, and the lateral confinement level $\frac{\sigma_3}{f_c'}$. With an increase of the lateral confining pressure σ_3, the axial strains at peak stress for both HSC and SFHSC increase remarkably, which can be illustrated by the following:

$$\text{HSC:}\quad \frac{\varepsilon_{1c}}{\varepsilon_{cu}} = 1 + 19.21\left(\frac{\sigma_3}{f_c'}\right) \quad (5)$$

$$\text{SFHSC:}\quad \frac{\varepsilon_{1c}}{\varepsilon_{cu}} = 1 + 17.33\left(\frac{\sigma_3}{f_c'}\right) \quad (6)$$

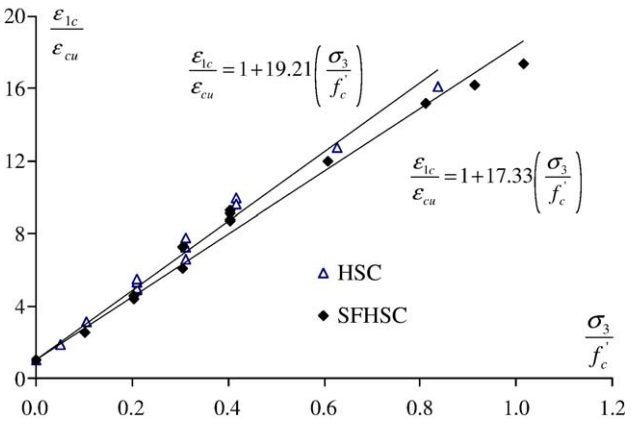

Fig. 17. $\frac{\varepsilon_{1c}}{\varepsilon_{cu}} - \frac{\sigma_3}{f_c'}$ relationships for HSC and SFHSC under triaxial compression.

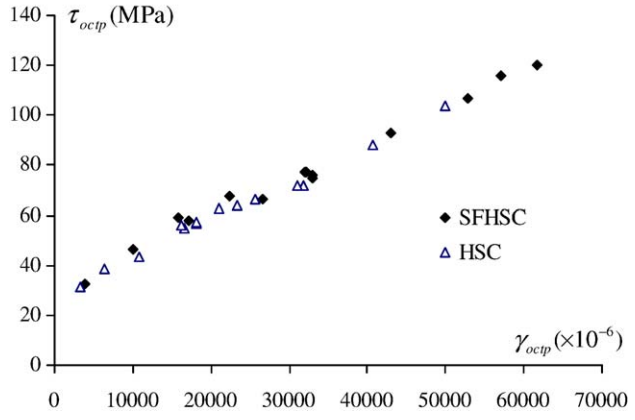

Fig. 18. τ_{octp}–γ_{octp} relations for HSC and SFHSC in triaxial compression.

For HSC, Eq. (5) is quite close to the result of Candappa et al. [11], where $\frac{\varepsilon_{1c}}{\varepsilon_{cu}} = 1 + 20\left(\frac{\sigma_3}{f'_c}\right)$, but will provide more ductility than the finding of Ansari and Li [2], where $\frac{\varepsilon_{1c}}{\varepsilon_{cu}} = 1 + 15.15\left(\frac{\sigma_3}{f'_c}\right)$.

3.2.4. Peak octahedral shear stress–strain relationship

The results of this study indicate that under triaxial compression, a strong relationship between τ_{octp} and γ_{octp} exists for both HSC and SFHSC, where τ_{octp} and γ_{octp} denote the octahedral shear stress and the engineering octahedral shear strain at the peak axial stress σ_{1c}, respectively. This relationship is shown in Fig. 18 and can be expressed as Eq. (7) for SFHSC and Eq. (8) for HSC:

$$\text{SFHSC:} \quad \tau_{octp} = 1.456 \times 10^3 \ \gamma_{octp} + 30.4 \tag{7}$$

$$\text{HSC:} \quad \tau_{octp} = 1.458 \times 10^3 \ \gamma_{octp} + 29.3 \tag{8}$$

It can be clearly seen from Fig. 18 that HSC and SFHSC behave essentially the same in terms of this relationship.

4. Conclusions

From this study, the following conclusions can be drawn:

- Under the uniaxial compression, the steel fiber reinforcement only slightly increased the uniaxial compressive strength and the peak axial and lateral strains of HSC, but notably improved its capability of resisting post peak deformation on the descending branch of the stress–strain curve.
- Under the triaxial compression, the steel fiber reinforcement has an insignificant effect on the nonlinear stress–strain relation of HSC.
- In the triaxial compression, the HSC and SFHSC essentially fall within the same ultimate strength envelops in terms of the Mohr-Coulomb and Willam-Warnke failure criteria.
- Under the triaxial compression, a uniform relationship between the octahedral shear stress and the engineering octahedral shear strain at peak stress can be adopted for both HSC and SFHSC.

Acknowledgment

The authors acknowledge the NSF grant #CMS 9413725, Material Testing System (1000 kip MTS 815) for Research and Development of High Performance Cementitious Composites provided to New Jersey Institute of Technology. This study would not have been possible without the availability of the machine funded by the above-mentioned grant.

References

[1] J. Xie, A.E. Elwi, J.G. MacGregor, Mechanical properties of three high-strength concretes containing silica fume, ACI Materials Journal 92 (2) (1995 (March/April)) 135–145.
[2] F. Ansari, Q. Li, High strength concrete subjected to triaxial compression, ACI Materials Journal 95 (6) (1998 (November/December)) 747–755.
[3] I. Imran, S.J. Pantazopoulou, Experimental study of plain concrete under triaxial stress, ACI Materials Journal 93 (6) (1996 (Nov./Dec.)) 589–601.
[4] J.C. Chern, H.J. Yang, H.W. Chen, Behavior of steel fiber reinforced concrete in multiaxial loading, ACI Materials Journal 89 (1) (1992 (Jan./Feb.)) 32–39.
[5] T. Ishikawa, H. Ohnuma, K. Izumo, S. Ohara, A mathematical description of deformational behavior of high strength concrete reinforced with steel fiber under triaxial compression, Transaction of the Japan Concrete Institute 22 (2000) 221–228.
[6] Z.H. Guo, Strength and Deformation of Concrete – Experimental Principles and Constitutive Law, Tsinghua University Press House, Beijing, P.R. China, 1997.
[7] J.G.M. Van Mier, S.P. Shah, et al., Strain softening of concrete in uniaxial compression, Materials and Structures 30 (1997 (May)) 195–209.
[8] S. Mindess, J.F. Young, D. Darwin, Concrete, second edition, Prentice Hall, New Jersey, USA, 2002.
[9] X. Lu, Uniaxial and Triaxial Behavior of High strength Concrete With and Without Steel Fibers, PhD Dissertation, Department of Civil and Environmental Engineering, New Jersey Institute of Technology, Newark, USA, January 2005.
[10] W.F. Chen, Plasticity in Reinforced Concrete, McGraw-Hill Book Company, New York, USA, 1982.
[11] D.C. Candappa, J.G. Sanjayan, S. Setunge, Complete stress–strain curves of high strength concrete, Journal of Materials in Civil Engineering 13 (3) (2001 (May/June)) 209–215.
[12] S. Lan, Z. Guo, Experimental investigation of multiaxial compressive strength of concrete under different stress paths, ACI Materials Journal 94 (5) (1997 (September/October)) 427–434.